A Novel Chaotic Map Based on Decay Functions and Its Applications

Pei Ding[1], Shivakumar Rajagopal[2], Sajad Jafari[3],
Kehui Sun[1], and Huihai Wang[1,*]

[1]School of Physics, Central South University, Changsha 410083, China

[2]Center for Cognitive Science, Trichy SRM Medical College Hospital and Research Center, Trichy 621105, India

[3]Health Technology Research Institute, Amirkabir University of Technology (Tehran Polytechnic), Tehran 15875-4413, Iran

August 19, 2026

Abstract

Motivated by decay-modulated nonlinear perturbations in discrete dynamical systems, this paper proposes a one-dimensional Sine-Bessel chaotic map by coupling the sine map with the zeroth-order Bessel function of the first kind. Fixed-point analysis establishes a bounded positively invariant interval, guarantees the existence of at least one fixed point, and provides a local stability criterion. Numerical investigations based on attractors, bifurcation diagrams, Lyapunov exponents, spectral entropy, and autocorrelation demonstrate that the map exhibits broad chaotic parameter regions and reduced periodic windows compared with the classical Sine map. Under synchronous translation of the two phase parameters, recurrent yet nonidentical bifurcation and Lyapunov-exponent structures are observed, revealing parameter-translation symmetry breaking caused by the nonperiodic decay term. Further comparisons among different decay functions show that the fixed-translation difference determines the persistence of structural deformation, while oscillation governs its alternating form. Finally, a pseudorandom number generator is constructed, and its output passed the adopted NIST SP 800-22 statistical criteria.

Keywords: chaotic map; Bessel function; parameter-translation symmetry breaking; dynamical characteristics; pseudorandom number generator

PACS: 05.45.-a, 05.45.Ac

1. Introduction

One-dimensional discrete maps are mathematically simple yet capable of generating fixed-point destabilization, period-doubling bifurcations, periodic windows, chaotic bands, and complex parameter-space structures, making them valuable models for investigating the fundamental mechanisms of nonlinear dynamics [1–4]. Their

*Corresponding author. E-mail: wanghuihai_csu@csu.edu.cn

iterative forms are also simple, computationally inexpensive, and convenient for digital implementation. Consequently, they have potential applications in pseudorandom sequence generation [5,6], information security [7,8], and digital signal processing [9,10]. Recent developments have further extended complex discrete and memristive dynamics to neural-network modeling and emerging applications such as brain-inspired computing and time-series forecasting [11,12]. Introducing additional nonlinear terms into classical maps can alter local stretching, folding, and the distribution of critical points, thereby reorganizing their bifurcation structures. Existing studies have employed nonlinear control [13,14], multi-map cascading [15], delayed feedback [16], memristive coupling [17,18], and nonlinear transformations [19–21] to expand chaotic parameter intervals, reduce periodic windows, and increase orbital complexity. For example, Logistic-Sine coupling can modify the bifurcation structure of classical maps [22], while feedback control, offset enhancement, and memristive coupling can also broaden chaotic regions or increase state complexity [18,23]. In addition, trigonometric functions, special functions, and composite functions have been used to construct new discrete maps with complex dynamical behaviors [24–26]. These studies demonstrate that additional nonlinear terms provide an important means of regulating the dynamics of low-dimensional maps.

The additional terms used in existing discrete maps exhibit various spatial structures, including constant-amplitude periodic modulation, general aperiodic nonlinear terms, monotonically decaying terms, and decaying oscillatory terms [15,27]. Different perturbations differ substantially in periodicity, sign variation, amplitude evolution, and spatial range of influence, and may therefore affect the parameter dependence of a map family in different ways. A constant-amplitude periodic term has a well-defined translation period, and its geometric form possesses an exact repetitive basis under the corresponding parameter translation [28–30]. A general aperiodic term can break such regularity, although the resulting structural variation often lacks a unified asymptotic description [14,31]. A monotonically decaying term mainly changes the local geometry near the perturbation center, and its influence gradually weakens with increasing spatial distance [32,33]. A decaying oscillatory term, however, combines persistent sign alternation with a varying amplitude envelope and therefore exhibits both repeated local modulation and global amplitude evolution [34]. Despite these substantial structural differences, existing studies generally treat additional terms primarily as tools for expanding chaotic regions, increasing Lyapunov exponents (LEs), or enhancing complexity. Comparatively little attention has been devoted to how the periodicity, oscillation, and decay of a perturbation determine the repetition and evolution of dynamical structures under parameter translation from the perspective of an entire map family.

To address this research gap, this paper introduces a decaying oscillatory perturbation into the one-dimensional sine map by coupling it with the zeroth-order Bessel function of the first kind. The resulting map is first examined to determine whether the additional nonlinear term can broaden chaotic parameter regions, reduce periodic windows, and enhance dynamical complexity. The analysis is then extended from the dynamics of individual orbits to the parameter-space structure of the map family, with particular emphasis on how the decaying oscillatory term breaks the exact parameter-translation symmetry inherited from the periodic sine component. The function $J_0(u)$ is bounded and aperiodic, and it oscillates between positive and negative values with an amplitude decaying as $O(|u|^{-1/2})$ [34,35]. Compared with rapidly damped oscillatory perturbations and the sinc function, this relatively slow algebraic decay allows the oscillatory modulation of $J_0(u)$ to remain appreciable over a broader spatial range. These properties make $J_0(u)$ particularly suitable

for investigating both chaos enhancement and the persistent, decay-induced evolution of parameter-dependent dynamical structures under parameter translation.

Accordingly, the study first establishes the boundedness, fixed-point existence, and local stability properties of the proposed map. Its dynamical behavior is then characterized using attractor analysis, bifurcation diagrams, LE, two-dimensional parameter planes, spectral entropy (SE), and correlation analysis. Subsequently, synchronous translation of the two phase parameters is employed to reveal recurrent yet nonidentical bifurcation and LE structures and to clarify the mechanism of parameter-translation symmetry breaking. This mechanism is further generalized to periodic base functions coupled with decay terms, and several representative decay laws are compared in terms of their fixed-translation differences. Finally, a pseudorandom number generator (PRNG) is developed and evaluated using the NIST SP 800-22 test suite.

The rest of this paper is organized as follows. Section 2 introduces the Bessel function and constructs the Sine-Bessel map. Section 3 analyzes its dynamical characteristics. Section 4 investigates parameter-translation symmetry and its breaking mechanism. Section 5 presents the PRNG design and statistical evaluation, and Section 6 concludes the paper.

2. Chaotic map based on a decay function

2.1. Characteristics of the Bessel function

The Bessel functions originate from the solution of classical partial differential equations. Specifically, when applying the method of separation of variables to solve the wave equation, Laplace's equation, and the Helmholtz equation in cylindrical coordinates [35], a specific ordinary differential equation is naturally derived. Bessel functions are exactly standard solutions to this equation [34], which is defined as

$$x^2\frac{d^2y}{dx^2} + x\frac{dy}{dx} + (x^2 - \alpha^2)y = 0, \tag{1}$$

where α denotes the order of the Bessel function. In the chaotic map proposed in this paper, special attention is given to the case $\alpha = 0$. When $\alpha = 0$, the solution of Eq. (1) that remains finite at the origin is called the zeroth-order Bessel function of the first kind, usually denoted by $J_0(\cdot)$ [35]. Although this function is defined by an infinite series, its integral representation more intuitively reveals its internal modulation behavior and is given by

$$J_0(u) = \frac{1}{\pi}\int_0^{\pi} \cos(u\sin\theta)d\theta. \tag{2}$$

As shown in Fig. 1, the curve of $J_0(u)$ is regarded as a decaying cosine-like function. Its essential features may be summarized in two aspects. First, it exhibits aperiodic decaying oscillation, with repeated alternation between positive and negative values resembling a cosine waveform. Second, it has an asymptotic attenuation property: as $|u|$ increases, the oscillation amplitude is constrained by the envelope $\pm\sqrt{2/(\pi|u|)}$ which gradually converges to zero.

2.2. Construction of the Sine-Bessel map

In a one-dimensional discrete map, introducing different nonlinear terms changes the stretching, folding, and local-extremum distribution of the map curve. In this paper, the strictly periodic sine function is coupled

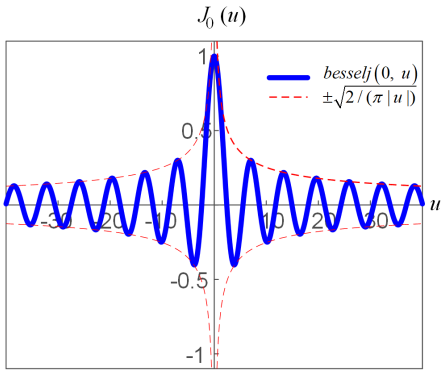


Figure 1: Zeroth-order Bessel function of the first kind, $J_0(u)$.

with the aperiodic decaying oscillation of the Bessel function, yielding

$$x_{n+1} = A\sin[\pi(x_n - a)] + BJ_0(x_n - b), \tag{3}$$

where A and B control the amplitudes of the sine and Bessel components, respectively, while a and b control their horizontal translations in the state space. Equation (3) is referred to as the Sine-Bessel chaotic map. The block diagram of this chaotic map structure is shown in Fig. 2. For convenience, the map function on the right-hand side of Eq. (3) is denoted by $f_{a,b}(x)$.

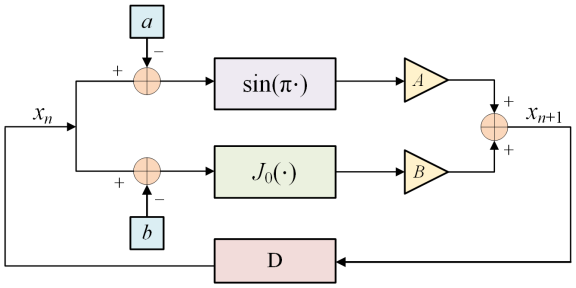


Figure 2: Structural block diagram of the Sine-Bessel map.

Parameters A and B determine the relative weights of the two nonlinear components. Increasing A strengthens the periodic folding generated by the sine component, whereas increasing B strengthens the modulation of the map geometry by the Bessel perturbation. Parameter a translates only the sine component, while parameter b translates only the Bessel component. By adjusting the four parameters, the map exhibits different geometric structures and dynamical properties.

3. Dynamical analysis

3.1. Stability analysis

3.1.1. Existence of the fixed points

A fixed point x^* of the Sine-Bessel map satisfies

$$x^* = A\sin\left[\pi(x^* - a)\right] + BJ_0(x^* - b). \tag{4}$$

Define the auxiliary function

$$H(x) = A\sin\left[\pi(x - a)\right] + BJ_0(x - b) - x. \tag{5}$$

Theorem 1. *The range of the Sine-Bessel map is contained in the closed interval*

$$I_{A,B} = \left[-\left(|A| + |B|\right), |A| + |B|\right]. \tag{6}$$

This interval is positively invariant, and the map has at least one fixed point in this interval, and all fixed points lie in $I_{A,B}$.

Proof. When $|\sin(\cdot)| \leq 1$ and $|J_0(\cdot)| \leq 1$, for $x \in \mathbb{R}$, then we have

$$|f_{a,b}(x)| \leq |A| + |B|. \tag{7}$$

Therefore, every initial state enters $I_{A,B}$ after one iteration and remains in this interval thereafter. At the two endpoints,

$$H(|A| + |B|) = f_{a,b}(|A| + |B|) - (|A| + |B|) \leq 0, \tag{8}$$

and

$$H(-|A| - |B|) = f_{a,b}(-|A| - |B|) + |A| + |B| \geq 0. \tag{9}$$

Since $H(x)$ is continuous, the intermediate value theorem guarantees the existence of at least one $x^* \in I_{A,B}$ such that $H(x^*) = 0$. □

From the graphical fixed-point criterion, parameters A and B control the vertical amplitude and local fluctuations of the map curve. As either A or B increases, the map curve may intersect the diagonal $y = x$ more frequently, although the number of fixed points does not necessarily increase monotonically with either parameter. Parameters a and b translate the sine and Bessel components, respectively, changing the positions of local extrema relative to the diagonal and thereby potentially changing the number and distribution of fixed points.

Figure 3 illustrates the regulation of fixed points by plotting the intersections of $y = f_{a,b}(x)$ and $y = x$. The relatively small amplitudes in Fig. 3(a) produce a limited number of intersections. When either A or B is increased, the amplitude and local geometry of the map curve change substantially, resulting in corresponding changes in the number or locations of the fixed points. Figure 3(d) shows that translating the sine component changes the locations of local peaks and valleys relative to the diagonal, thereby modifying the intersection structure.

3.1.2. Local stability of the fixed points

For the Sine-Bessel chaotic map, the local stability of a fixed point is determined by the derivative multiplier. The derivative of Eq. (3) is

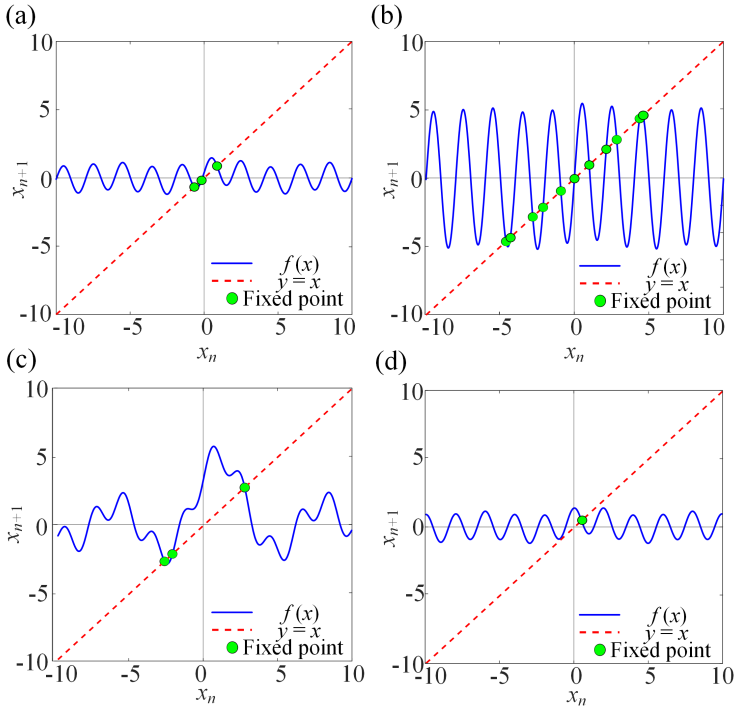


Figure 3: Effects of amplitude and phase parameters on the fixed-point distribution. (a) $A = 1$, $B = 0.5$, $a = 0$, and $b = 1$, (b) $A = 5$, $B = 0.5$, $a = 0$, and $b = 1$, (c) $A = 1$, $B = 5$, $a = 0$, and $b = 1$, (d) $A = 1$, $B = 0.5$, $a = 1.5$, and $b = 1$.

$$f'_{a,b}(x) = A\pi \cos\left[\pi(x-a)\right] - BJ_1(x-b), \tag{10}$$

where $J_1(\cdot)$ is the Bessel function of the first kind and order one. At a fixed point x^*, the multiplier is

$$\lambda = A\pi \cos\left[\pi(x^*-a)\right] - BJ_1(x^*-b). \tag{11}$$

The fixed point is locally asymptotically stable when $|\lambda| < 1$ and unstable when $|\lambda| > 1$. When $|\lambda| = 1$, the fixed point is nonhyperbolic, and the linearized criterion alone cannot determine its stability; higher-order nonlinear terms must then be considered [36].

Since $J_1(\cdot)$ is continuous on the bounded interval $I_{A,B}$, its absolute value has a finite maximum there. By the reverse triangle inequality, the multiplier at a fixed point satisfies

$$\begin{aligned} |\lambda| &= |A\pi \cos[\pi(x^*-a)] - BJ_1(x^*-b)| \\ &\geq |A|\pi\,|\cos[\pi(x^*-a)]| - |B| \max_{x\in I_{A,B}} |J_1(x-b)|. \end{aligned} \tag{12}$$

Therefore, if

$$|A|\pi\,|\cos[\pi(x^*-a)]| > 1 + |B| \max_{x\in I_{A,B}} |J_1(x-b)|, \tag{13}$$

then $|\lambda| > 1$, and the corresponding fixed point is locally unstable. Conversely, for $A \neq 0$, if a fixed point satisfies $|\lambda| < 1$, it must satisfy

$$|\cos[\pi(x^* - a)]| < \frac{1 + |B| \max\limits_{x \in I_{A,B}} |J_1(x - b)|}{|A|\pi}. \tag{14}$$

For the special case $A = 0$, the multiplier reduces to $\lambda = -BJ_1(x^* - b)$. Hence, the fixed point is locally asymptotically stable when $|BJ_1(x^* - b)| < 1$, unstable when $|BJ_1(x^* - b)| > 1$, and nonhyperbolic when $|BJ_1(x^* - b)| = 1$.

For $A \neq 0$, Equation (14) shows that the contribution of the sine derivative scales with $|A|\pi$. When this quantity is large compared with the maximum possible magnitude of the Bessel derivative term, the sine derivative must itself remain small for a fixed point to be stable. Consequently, any stable fixed point, if one exists, is typically confined to a narrow phase interval near $x^* - a \approx k + \frac{1}{2}, k \in \mathbb{Z}$, where the derivative of the sine component is close to zero. A stable fixed point outside these intervals is possible only if the sine and Bessel derivative terms have the same sign and comparable magnitudes, so that they strongly cancel in the multiplier. Therefore, increasing $|A|$ substantially narrows the possible phase region of a stable fixed point. By contrast, the influence of B is not monotonic. Depending on the phase and parameter values, the Bessel derivative term may either enhance local stretching or reduce $|\lambda|$ through cancellation with the sine derivative term.

To further characterize the fixed-point stability regions beyond the analytical restrictions above, a numerical scan was performed on the A–B parameter plane with $a = 0$ and $b = 1$. The fixed-point stability boundary is determined jointly by the fixed-point equation and the condition $|\lambda| = 1$, and the numerical scan provides a direct approximation of this boundary in the selected parameter plane. For each parameter pair, all fixed points in the invariant interval $I_{A,B}$ were numerically determined and classified according to the multiplier condition $|\lambda| < 1$. Figure 4(a) shows the number of locally stable fixed points, indicating that stable fixed points occur only within specific parameter regions, while broad regions contain exclusively unstable fixed points. Figure 4(b) further shows the fixed-point branches for $B = 0.5$, illustrating the creation and evolution of stable and unstable branches and their transitions near $|\lambda| = 1$.

For all fixed points reported for the representative parameter sets in Table 1, however, $|\lambda| > 1$. These fixed points are therefore locally repelling, providing a local dynamical mechanism for orbital stretching, folding, and complex iterative behavior.

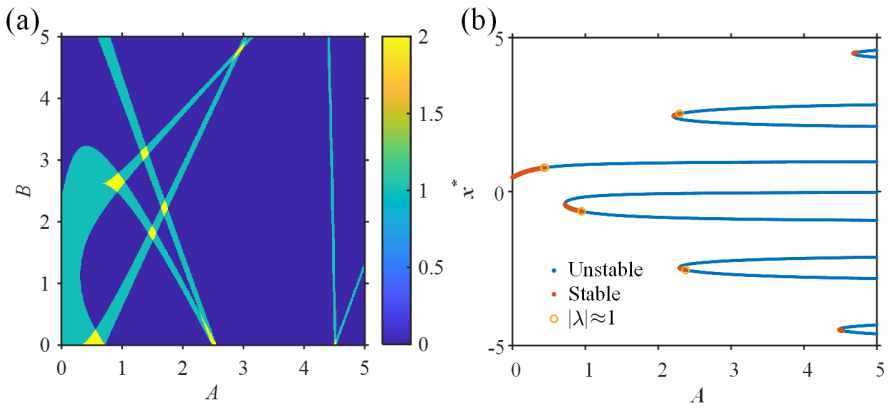


Figure 4: Numerical fixed-point stability analysis of the Sine-Bessel map with $a = 0$ and $b = 1$. (a) Number of locally stable fixed points on the A–B parameter plane. (b) Fixed-point branches versus A for $B = 0.5$, showing stable and unstable branches together with the approximate stability boundaries $|\lambda| = 1$.

Table 1: Representative fixed-point stability results for the selected parameter sets.

(A, B, a, b)	Fixed point x^*	$\lvert\lambda\rvert$	Stability
$(1, 0.5, 0, 1)$	-0.6626	1.2481	Unstable
	-0.1720	2.9394	Unstable
	0.8765	2.8772	Unstable
$(1, 5, 0, 1)$	-2.7380	1.9458	Unstable
	-2.2040	3.8170	Unstable
	2.7170	4.8734	Unstable
$(5, 1, 0, 1)$	-4.6193	6.0843	Unstable
	-4.3242	7.8940	Unstable
	-2.8381	13.7214	Unstable

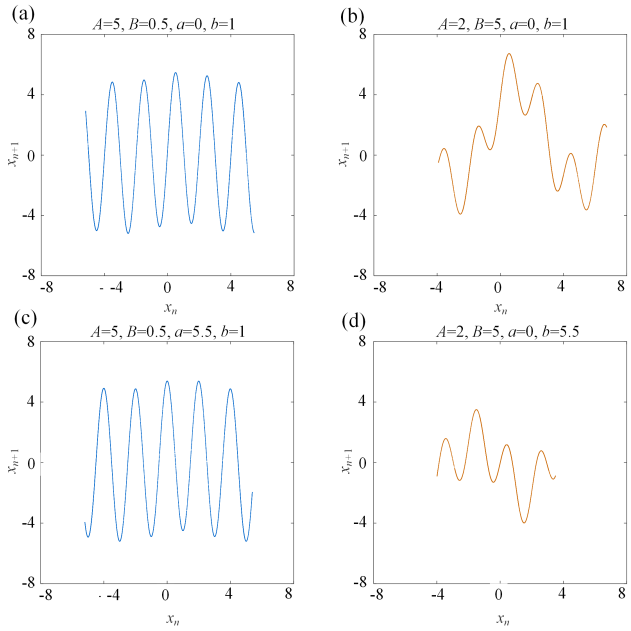


Figure 5: Phase space attractors of the Sine-Bessel map in the (x_n, x_{n+1}) plane. (a) $A = 5$, $B = 0.5$, $a = 0$, and $b = 1$; (b) $A = 2$, $B = 5$, $a = 0$, and $b = 1$; (c) $A = 5$, $B = 0.5$, $a = 5.5$, and $b = 1$; and (d) $A = 2$, $B = 5$, $a = 0$, and $b = 5.5$.

3.2. Attractor analysis

With the initial condition $x_0 = 0.1$, the first-return plots under different parameter settings are shown in Fig. 5. When $A = 5$ and $B = 0.5$, as shown in Fig. 5(a), the sine component is dominant, and the first-return plot retains a pronounced sine-like folded outline. When the weight of the Bessel component is increased to $B = 5$, as shown in Fig. 5(b), the map curve is subjected to stronger aperiodic decay modulation, and its local fluctuations and spatial distribution change more substantially.

The phase parameters control the horizontal positions of the two nonlinear components. By comparing Figs. 5(a) and 5(c), it can be seen that changing a shifts the sine component and changes the distribution of the orbit. Similarly, Figs. 5(b) and 5(d) show that changing b shifts the Bessel component and changes the region where the aperiodic modulation affects the dynamics. Therefore, a and b control the positions of the periodic

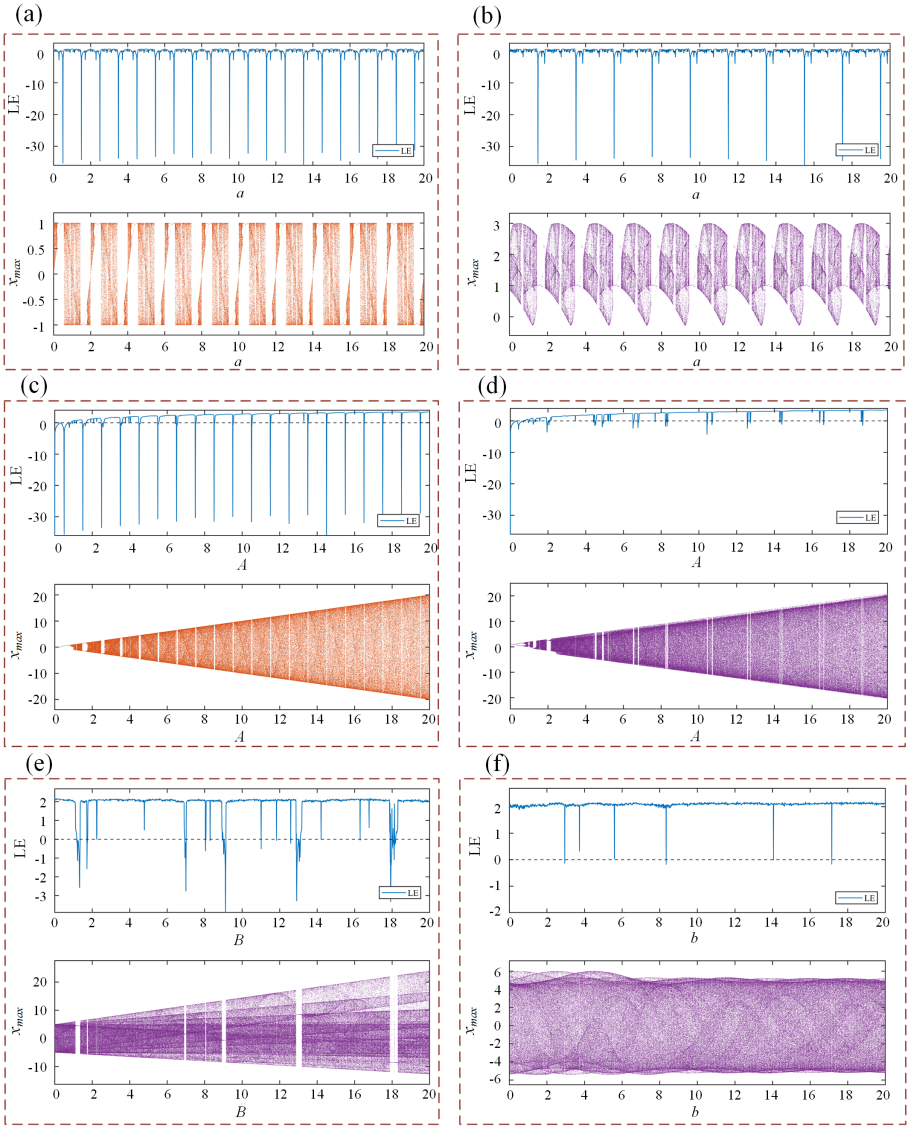


Figure 6: Bifurcation diagrams and LE spectra of the sine map and the Sine-Bessel map under different parameter variations. (a) Sine map versus a; (b) Sine-Bessel map versus a; (c) sine map versus A; (d) Sine-Bessel map versus A; (e) Sine-Bessel map versus B; and (f) Sine-Bessel map versus b. For each parameter value, the map is iterated for 10^5 steps, and the first 8×10^4 iterations are discarded to eliminate transient effects.

and decaying components, respectively.

3.3. Bifurcation and LE

3.3.1. Bifurcation and LE under parameter variations

To compare the dynamical characteristics of the Sine-Bessel map with those of the classical sine map, the initial condition is fixed at $x_0 = 0.1$. For $A = 1$, $B = 2$, $b = 1$, and $a \in [0, 20]$, the Lyapunov exponent spectra and bifurcation diagrams of the two maps with respect to the phase parameter a are shown in Figs. 6(a) and 6(b), respectively. It can be observed that the Sine-Bessel map exhibits fewer pronounced periodic windows within the investigated parameter range and a broader chaotic region.

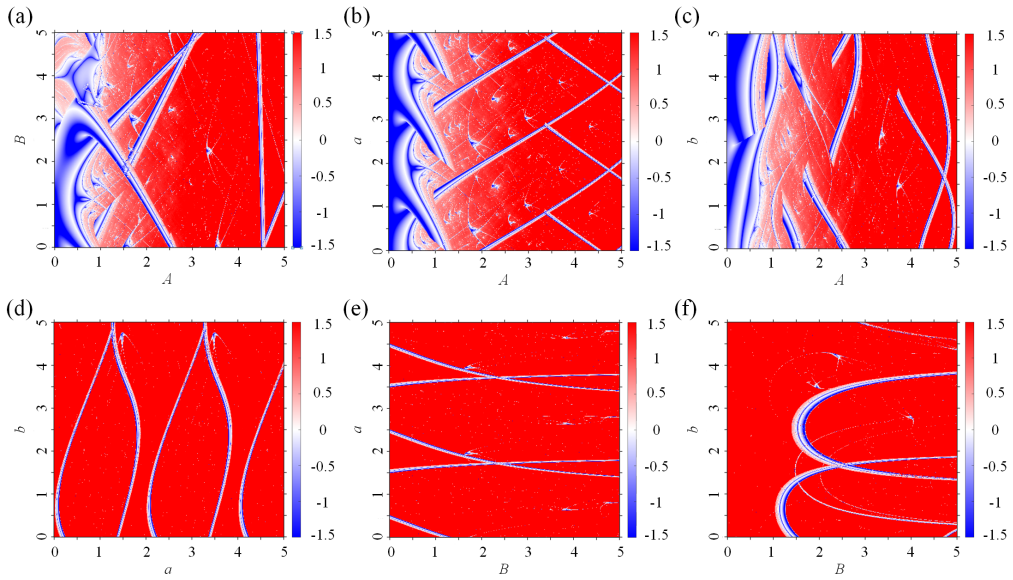


Figure 7: LE distributions on different parameter planes. (a) A–B plane with $(a, b, x_0) = (0, 1, 0.1)$; (b) A–a plane with $(B, b, x_0) = (1, 1, 0.1)$; (c) A–b plane with $(a, B, x_0) = (0, 1, 0.1)$; (d) a–b plane with $(A, B, x_0) = (5, 1, 0.1)$; (e) B–a plane with $(A, b, x_0) = (5, 1, 0.1)$; and (f) B–b plane with $(A, a, x_0) = (5, 0, 0.1)$. For each parameter plane, both parameters are scanned in steps of 0.01, and the LE is calculated from the last 2×10^4 of 10^5 iterations after discarding the first 8×10^4 as transients.

Additionally, setting $B = 2$, $a = 0$, $b = 1$, and $A \in [0, 20]$, the comparisons of the LE spectra and bifurcation diagrams concerning the amplitude parameter A are plotted in Figs. 6(c) and 6(d). Compared with the classical sine map, the addition of the Bessel perturbation substantially reorganizes the bifurcation structure and LE spectrum. Within the investigated parameter range, the Sine-Bessel map exhibits a broader positive-LE interval and fewer clearly visible periodic windows. Furthermore, to comprehensively assess the effect of the Bessel perturbation term, bifurcation diagrams and LE spectra are also plotted with respect to the amplitude parameter B (setting $A = 5$, $a = 0$, $b = 1$) and the phase parameter b (setting $A = 5$, $B = 1$, $a = 0$), as shown in Fig. 6(e) and Fig. 6(f). As B increases, the LE remains positive over most of the interval, with pronounced decreases and narrow periodic windows occurring only near a small number of parameter values. As b varies, the orbit distribution remains dense and changes smoothly, with positive LE values prevailing over most of the interval. These results demonstrate that the map remains chaotic over a wide parameter range and thus possesses superior chaotic performance.

To further examine the interactions among the four parameters (A, B, a, b), Fig. 7 presents six two-dimensional LE spectra for different parameter pairs. In these contour maps, the red regions correspond to LE > 0 and therefore indicate chaotic dynamics. The extensive red regions observed across the six parameter planes show that the Sine-Bessel map maintains chaotic behavior over broad parameter combinations, indicating strong dynamical robustness within the investigated parameter ranges.

3.3.2. Symmetry breaking in bifurcation and LE structures

To examine the effect of simultaneous phase translation, we set $a = b = \mu$, where $\mu \in [0, 20]$, and take $x_0 = 0.1$. The bifurcation diagram and LE spectrum for $A = 1$ and $B = 0.5$ are shown in Fig. 8(a), while the corresponding results for $A = 1$ and $B = 1$ are shown in Fig. 8(b).

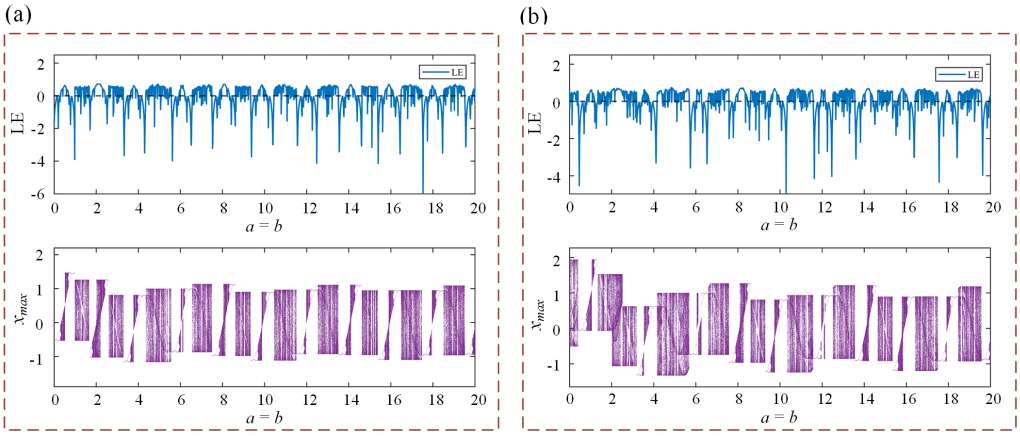


Figure 8: The LE spectra and bifurcation diagrams of the Sine-Bessel map under the coupled phase translation $a = b = \mu \in [0, 20]$ (a) $A = 1$, $B = 0.5$, (b) $A = 1$, $B = 1$.

Under the translation $\mu \to \mu + 2$, the sine component repeats exactly and therefore provides a period-2 parameter skeleton. In contrast, the Bessel component generally satisfies $J_0(x - \mu - 2) \neq J_0(x - \mu)$ and consequently does not repeat under the same translation. The complete map family therefore loses its exact period-2 parameter periodicity, although the bifurcation diagrams and LE spectra remain organized by the periodic skeleton inherited from the sine component. As a result, adjacent parameter intervals of length 2 exhibit repeated yet nonidentical dynamical structures.

This phenomenon is referred to here as parameter-translation symmetry breaking: the periodic component retains its translation symmetry, whereas the nonperiodic decaying oscillatory component breaks the corresponding symmetry of the complete map family. A systematic formulation of this mechanism, including its general conditions and asymptotic behavior, is presented in Section 4. As B increases, the map-level deviation introduced by the Bessel component is amplified, and the differences between adjacent nominal periods in the displayed bifurcation and LE structures generally become more pronounced. Moreover, because the amplitude of J_0 decays only as $O(|u|^{-1/2})$, the period-to-period deformation remains visible over a broad phase-translation interval. From an application perspective, exact parameter-translation symmetry may introduce dynamically equivalent or redundant parameter choices in parameterized chaotic systems. Breaking this exact symmetry removes such equivalence and may increase the distinguishability of parameter values and the diversity of the corresponding chaotic sequences, which may be useful for parameterized PRNGs and other chaos-based applications.

3.4. SE complexity analysis

SE is used to measure time-series complexity from the distribution of spectral energy in the frequency domain. A larger SE indicates that the power-spectrum energy is more broadly distributed and that the

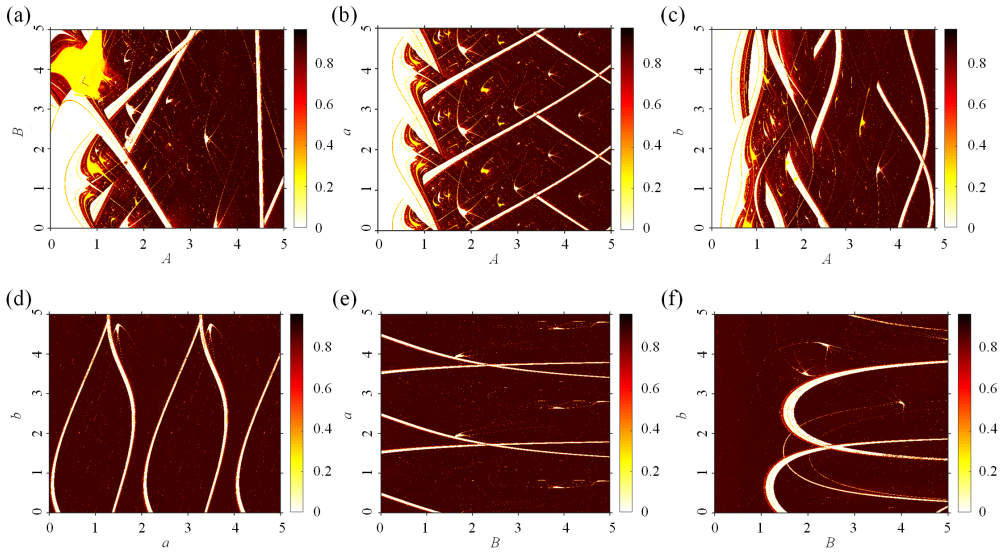


Figure 9: SE distributions of the Sine-Bessel map on different parameter planes. (a) A–B plane with $(a, b, x_0) = (0, 1, 0.1)$; (b) A–a plane with $(B, b, x_0) = (1, 1, 0.1)$; (c) A–b plane with $(a, B, x_0) = (0, 1, 0.1)$; (d) a–b plane with $(A, B, x_0) = (5, 1, 0.1)$; (e) B–a plane with $(A, b, x_0) = (5, 1, 0.1)$; and (f) B–b plane with $(A, a, x_0) = (5, 0, 0.1)$. For each parameter plane, both parameters are scanned in steps of 0.01, and the SE is calculated from the last 2×10^4 of 10^5 iterations after discarding the first 8×10^4 as transients.

frequency-domain structure is generally more complex [37].

As shown in Fig. 9, most parameter regions have high SE, indicating that the orbits generally have broadly distributed power-spectrum energy and high frequency-domain complexity. Some band-shaped or curved regions exhibit substantially lower SE and correspond closely to the nonchaotic regions in Fig. 7. It indicates that when the system enters a periodic window or critical state, its spectral energy tends to concentrate in a small number of frequency components, resulting in a decrease in SE. The exponential separation of nearby trajectories and the broad power-spectrum distribution jointly demonstrate that the Sine-Bessel map exhibits robust and complex dynamics over broad parameter ranges.

3.5. Correlation analysis

Autocorrelation is an important statistical indicator for evaluating the temporal randomness and linear correlation of chaotic sequences [38]. For an ideal pseudorandom sequence, the autocorrelation function should approximate a Dirac delta function; that is, the sequence should be highly correlated only at zero lag and essentially uncorrelated at all nonzero lags [39]. To eliminate the influence of the sequence mean and amplitude, the mean-removed and normalized sample autocorrelation is adopted. For nonnegative lags, it is defined as

$$\rho(m) = \frac{\sum_{i=1}^{n-m} (u_i - \bar{u})(u_{i+m} - \bar{u})}{\sqrt{\sum_{i=1}^{n-m} (u_i - \bar{u})^2 \sum_{i=1}^{n-m} (u_{i+m} - \bar{u})^2}}, \qquad m \geq 0, \tag{15}$$

where u denotes the sequence, and $\bar{u}$ is its sample mean. n and m denote the sequence length and the lag, respectively. The autocorrelation at negative lags is obtained from the symmetry relation $\rho(-m) = \rho(m)$, and the normalization gives $\rho(0) = 1$. For the autocorrelation analysis, the sequence length is $n = 10^5$, the first 8×10^4 iterations are discarded as transients, and the maximum lag is set to 2000. The approximate pointwise 95% confidence bounds for white noise are given by $\pm 1.96/\sqrt{n}$.

As shown in Fig. 10, both autocorrelation functions have a pronounced peak at $m = 0$ and rapidly decrease toward zero at nonzero lags. The maximum absolute nonzero-lag autocorrelation occurs at $m = 1$, with values of 0.1785 and 0.2815 for the Sine-Bessel map and the sine map, respectively. Thus, the introduction of the Bessel term reduces the dominant one-step linear correlation by approximately 36.6%. Beyond the short-lag region, the autocorrelation coefficients of both sequences fluctuate around zero, with most values lying within or close to the approximate confidence bounds. These results indicate that the Bessel perturbation reduces the short-range linear temporal dependence of the sine-map sequence under the tested parameter setting.

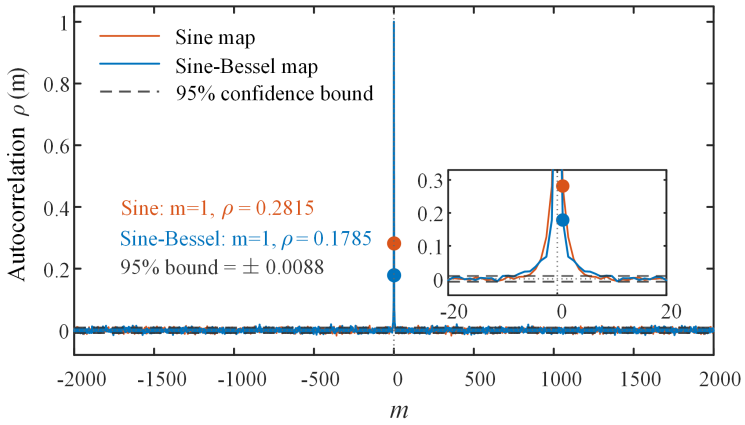


Figure 10: Comparison of the mean-removed and normalized sample autocorrelation functions of the sine map and the Sine-Bessel map. The inset shows an enlarged view of the short-lag region.

4. Parameter-translation symmetry and its breaking mechanism

The coupled phase scan in Section 3.3.2. reveals recurrent yet nonidentical bifurcation and LE structures. This section formulates the corresponding parameter-translation symmetry and explains its breaking mechanism at the map-family level.

4.1. Three phase-translation modes

Equation (3) is written as

$$f_{a,b}(x) = A \sin[\pi(x - a)] + B J_0(x - b). \tag{16}$$

When b is fixed, the identity $\sin[\pi(x - a - 2)] = \sin[\pi(x - a)]$ gives

$$f_{a+2,b}(x) = f_{a,b}(x), \tag{17}$$

so the map family is exactly period-2 for parameter a.

When a is fixed and only b varies, the parameter dependence is determined by the translation of $J_0(x-b)$. Since J_0 is nonperiodic, the map is generally not periodic for parameter b.

For synchronous translation, $a = b = \mu$, the map takes the form

$$f_\mu(x) = A\sin[\pi(x-\mu)] + BJ_0(x-\mu). \tag{18}$$

Under $\mu \to \mu + 2$, the sine component repeats exactly, whereas the Bessel component does not. Therefore, the exact period-2 parameter symmetry is broken, while the periodic skeleton inherited from the sine component remains.

4.2. Coupling of a general periodic function and a decay function

Consider the general map family

$$g_\mu(x) = F(x-\mu) + BD(x-\mu), \tag{19}$$

where F is a nonconstant function with period $P > 0$, $F(z-P) = F(z)$, $B \neq 0$, and $D \not\equiv 0$ satisfies $\lim_{|z|\to\infty} D(z) = 0$.

Theorem 2. *The map family g_μ is not globally and exactly P-periodic with respect to the parameter μ. Moreover, for every bounded state interval I,*

$$\lim_{|\mu|\to\infty} \sup_{x\in I} |g_{\mu+P}(x) - g_\mu(x)| = 0. \tag{20}$$

Proof. Using the periodicity property ($F(z-P) = F(z)$), we obtain

$$g_{\mu+P}(x) - g_\mu(x) = B\left[D(x-\mu-P) - D(x-\mu)\right]. \tag{21}$$

If $g_{\mu+P}(x) = g_\mu(x)$ for all x and μ, then, since $B \neq 0$, $D(z-P) = D(z)$ for every $z \in \mathbb{R}$. Thus, D is P-periodic. However, a periodic function satisfying $D(z) \to 0$ as $|z| \to \infty$ must be identically zero, contradicting $D \not\equiv 0$. Hence, the decay term breaks the global exact parameter periodicity.

For bounded I, both $x-\mu$ and $x-\mu-P$ tend uniformly to infinity in absolute value as $|\mu| \to \infty$. Therefore,

$$\sup_{x\in I} |D(x-\mu-P) - D(x-\mu)| \to 0,$$

Taking the supremum over $x \in I$ in Eq. (21) and using the uniform decay of the right-hand side as $|\mu| \to \infty$ directly yields Eq. (20). □

For the Sine-Bessel map, let $F(z) = A\sin(\pi z)$, $P = 2$, and $D(z) = J_0(z)$, then we have

$$f_{\mu+2}(x) - f_\mu(x) = B\left[J_0(x-\mu-2) - J_0(x-\mu)\right]. \tag{22}$$

Thus, adjacent nominal period-2 cells are generally nonidentical, although their map-level discrepancy decreases as $|\mu|$ increases. To quantify this discrepancy, we define

$$E_P(\mu; I) = \sup_{x \in I} |g_{\mu+P}(x) - g_\mu(x)| . \tag{23}$$

For the Sine-Bessel map,

$$E_2(\mu; I) = |B| \sup_{x \in I} |J_0(x - \mu - 2) - J_0(x - \mu)| . \tag{24}$$

A nonzero $E_2(\mu; I)$ indicates the breaking of exact period-2 parameter periodicity, whereas $E_2(\mu; I) \to 0$ as $|\mu| \to \infty$ describes its asymptotic recovery at the map-function level.

4.3. Effects of different decay functions on parameter periodicity

Consider the generalized map

$$x_{n+1} = A \sin [\pi(x_n - a)] + BD(x_n - b), \tag{25}$$

where $D(x)$ is a bounded decay function. This study compares the dynamical effects of five decay functions: exponential, Cauchy-type algebraic, sinc-type oscillatory, Bessel-type oscillatory, and LogSine-type oscillatory. Their waveforms are shown in Fig. 11. Under coupled phase translation, every nontrivial decay function destroys global exact parameter periodicity.

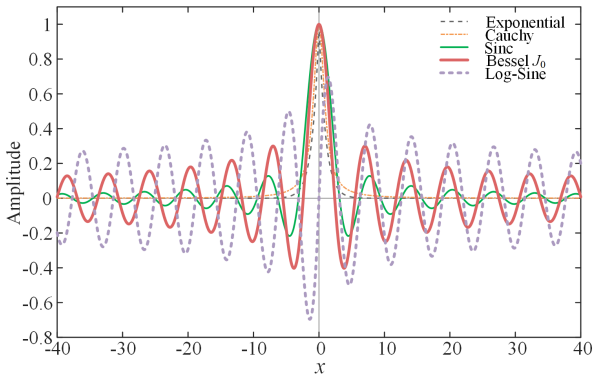


Figure 11: Waveform comparison of five representative decay functions.

Table 2: Comparison of different decay functions and their asymptotic fixed-translation properties.

Model	Decay function $D(u)$	Perturbation envelope	Typical asymptotic order of $D(u-2) - D(u)$	Structural effect
Sine-Bessel	$J_0(u)$	$O(\lvert u\rvert^{-1/2})$	Generally $O(\lvert u\rvert^{-1/2})$	Persistent alternating deformation
Sine-Exponential	$e^{-\alpha\lvert u\rvert}$, $\alpha > 0$	$O(e^{-\alpha\lvert u\rvert})$	$O(e^{-\alpha\lvert u\rvert})$	Rapid smooth weakening
Sine-Cauchy	$\dfrac{1}{1+u^2}$	$O(\lvert u\rvert^{-2})$	$O(\lvert u\rvert^{-3})$	Short-range smooth deformation
Sine-Sinc	$\dfrac{\sin(\pi u)}{\pi u}$	$O(\lvert u\rvert^{-1})$	$O(\lvert u\rvert^{-2})$	Localized alternating deformation
Sine-LogSine	$\dfrac{\sin u}{\ln(\lvert u\rvert + e)}$	$O(1/\ln \lvert u\rvert)$	Generally $O(1/\ln \lvert u\rvert)$	Long-range alternating modulation
Com-Sine-Bessel	$J_0(u)$	$O(\lvert u\rvert^{-1/2})$	Generally $O(\lvert u\rvert^{-1/2})$	Persistent nonidentical repetition

All maps coupled with the sine function in Table 2 are expressed in the form of Eq. (25). The composite-periodic-base-function model, denoted as the Com-Sine-Bessel map, is defined as

$$x_{n+1} = A\left[\sin\left(\pi(x_n - a)\right) + \frac{1}{3}\sin\left(3\pi(x_n - a)\right) + \frac{1}{5}\sin\left(5\pi(x_n - a)\right)\right] + BJ_0(x_n - b). \tag{26}$$

All three sine harmonics in Eq. (26) have the common period 2. Therefore, the Com-Sine-Bessel map retains an exact period-2 parameter skeleton.

According to Eq. (23), the following asymptotic conclusions are obtained directly for the different decay functions. For exponential decay, the far-field deviation satisfies $E_2(\mu; I) = O(e^{-\alpha|\mu|})$, and therefore the parameter-periodicity deviation vanishes most rapidly. For Cauchy decay, although the perturbation itself is $O(|\mu|^{-2})$, the difference between function values separated by a fixed distance of 2 is analogous to a first-order finite difference. Hence, $E_2(\mu; I) = O(|\mu|^{-3})$. For the sinc function, because $\frac{\sin[\pi(u-2)]}{\pi(u-2)} - \frac{\sin(\pi u)}{\pi u} = \frac{2\sin(\pi u)}{\pi u(u-2)}$. Therefore, $E_2(\mu; I) = O(|\mu|^{-2})$. For the LogSine function, translation by 2 changes both the sine phase and the slowly varying logarithmic denominator. In general, $E_2(\mu; I) = O\left(\frac{1}{\ln|\mu|}\right)$. For the Bessel function, a fixed translation by 2 generally does not cancel the leading oscillatory term. Consequently, $E_2(\mu; I) = O(|\mu|^{-1/2})$.

Therefore, the persistence of the structural deformation is quantified here by the fixed-translation discrepancy $E_2(\mu; I)$ and its asymptotic decay rate, rather than inferred solely from the visual appearance of the bifurcation structures. In particular, the Bessel case has $E_2(\mu; I) = O(|\mu|^{-1/2})$, which decays more slowly than the exponential, Cauchy, and sinc cases, while its oscillatory character produces an alternating deformation. The LogSine case decays even more slowly, confirming that the persistence is governed primarily by the decay law rather than being unique to the Bessel function.

4.4. Comparison of bifurcation structures and Lyapunov-exponent spectra

For the maps listed in Table 2, take $A = 1$, $B = 0.5$, and $x_0 = 0.1$, and let $a = b = \mu$ vary continuously. The results for exponential and Cauchy decay are shown in Fig. 12, and those for sinc and LogSine decay are shown in Fig. 13, and those for the Bessel and composite Sine-Bessel cases are shown in Fig. 14.

Although exponential and Cauchy terms also destroy exact period-2 parameter symmetry, their map-level deviations decay rapidly. As shown in Fig. 12, the complete maps therefore rapidly approach the period-2 parameter family determined by the pure sine component as μ increases. Since neither perturbation changes sign through oscillation, their far-field map deviation mainly exhibits a unidirectional and smooth weakening.

As shown in Fig. 13(a), the oscillatory deformation produced by the sinc term is mainly confined to the region near the perturbation center because its period-2 deviation decays as $O(|\mu|^{-2})$. In contrast, the slowly decaying LogSine term produces persistent sign-alternating modulation over a much broader parameter range, as reflected in both the bifurcation diagram and the LE spectrum in Fig. 13(b).

The Bessel term produces long-range structural deformation because its parameter-periodicity deviation decays slowly as $O(|\mu|^{-1/2})$. As shown in Fig. 14(b), repeated but nonidentical structures also remain when the sine base function is replaced by the composite periodic function in Eq. (26). This shows that parameter-translation symmetry breaking is not specific to a single sine waveform, but generally arises from coupling a periodic base function with an aperiodic decaying term.

In summary, coupling a periodic base function with a nonzero decaying term generally breaks exact parameter periodicity. The decay rate determines how long the resulting deformation persists, while the oscillatory

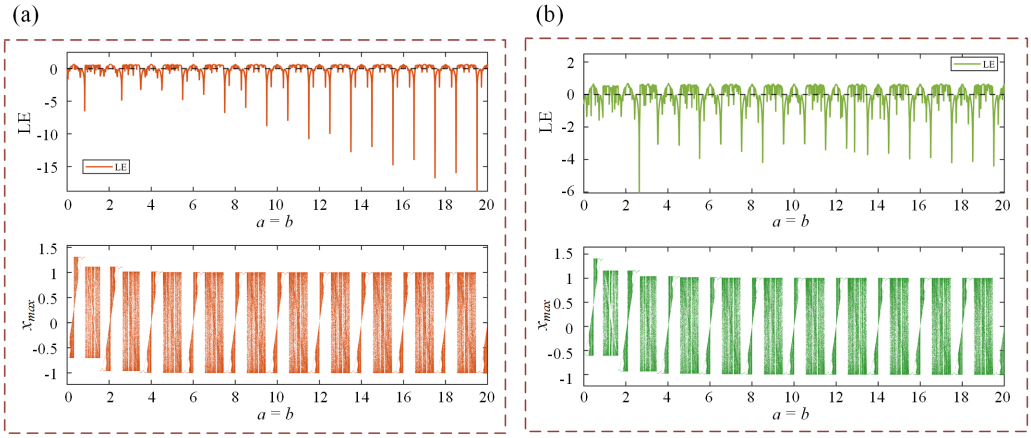


Figure 12: Bifurcation diagrams and LE spectra of the Sine-Exponential and Sine-Cauchy maps under the coupled phase translation $a = b = \mu$. (a) Sine-Exponential map; (b) Sine-Cauchy map.

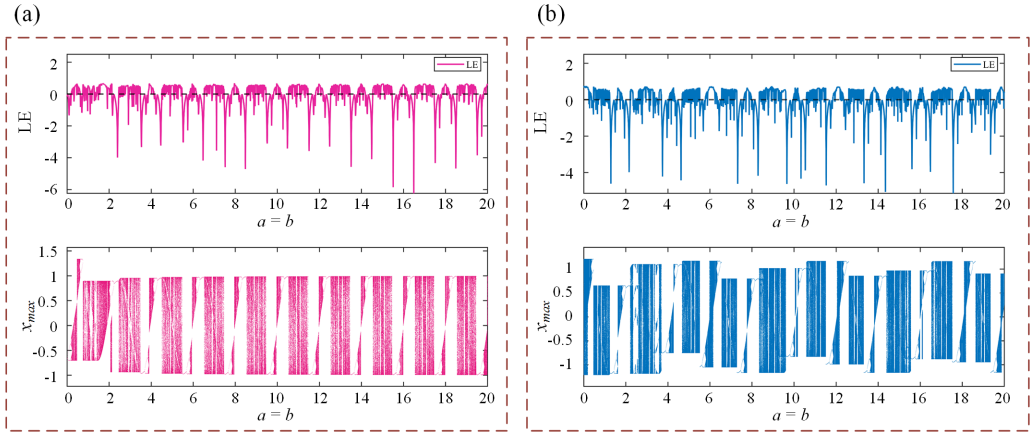


Figure 13: Bifurcation diagrams and LE spectra of the Sine-Sinc and Sine-LogSine maps under the coupled phase translation $a = b = \mu$. (a) Sine-Sinc map; (b) Sine-LogSine map.

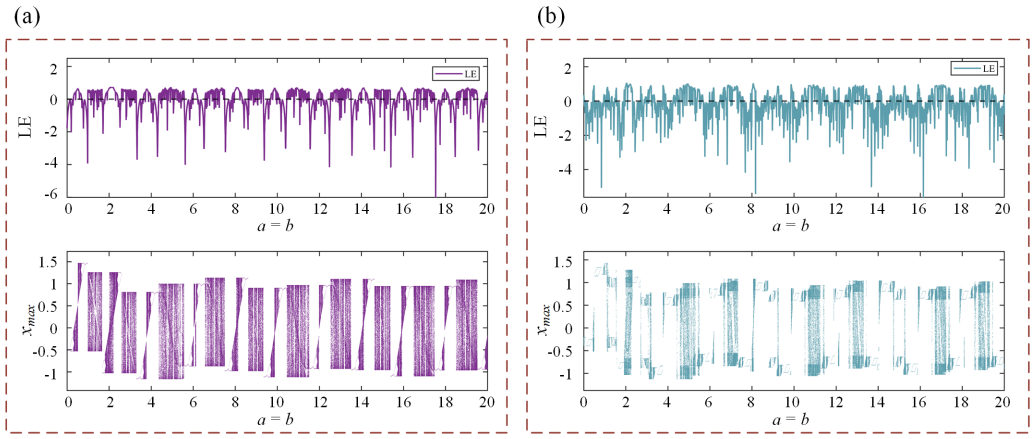


Figure 14: Bifurcation diagrams and LE spectra of the Sine-Bessel and Com-Sine-Bessel maps under the coupled phase translation $a = b = \mu$. (a) Sine-Bessel map; (b) Com-Sine-Bessel map.

behavior and phase relation control its sign alternation and geometric form. Slowly decaying oscillatory terms therefore produce the most persistent alternating modulation.

4.5. Effects of decay laws on structural repetition

The modulation of structural repetition by the decay function is further quantified. Under continuous variation of the coupled phase parameter, repeated bifurcation structures are typically accompanied by the reappearance of stable windows, critical regions, and chaotic regions along the parameter axis. Since the LE represents the mean stretching property at each parameter value as a scalar, correlations between different segments of an LE spectrum can be used to quantify the repetition of parameter-dependent structures.

To examine the effects of decay rate and oscillation frequency on this repeated structure, we consider the following exponentially and algebraically decaying oscillatory families:

$$D_{\exp}(u;\alpha,\omega) = e^{-\alpha|u|}\sin(\omega u), \qquad D_{\mathrm{alg}}(u;\gamma,\omega) = \frac{\sin(\omega u)}{(1+|u|)^{\gamma}}, \tag{27}$$

where ω denotes the oscillation frequency, while α and γ control the exponential and algebraic envelope-decay rates, respectively. Let $A = 1$, $B = 0.5$, $x_0 = 0.1$, and $a = b = \mu$. The LE sequence $L_i = \mathrm{LE}(\mu_i)$ is calculated over $\mu \in [0, 20]$.

To remove the effect of the mean LE level, define the mean-removed sequence $\widetilde{L}_i = L_i - \overline{L}$. The normalized autocorrelation at lag k and the Lyapunov-exponent-spectrum autocorrelation strength index (LASI) are defined as

$$R(k) = \frac{\sum_{i=1}^{M-k} \widetilde{L}_i \widetilde{L}_{i+k}}{\sum_{i=1}^{M} \widetilde{L}_i^2}, \qquad \mathrm{LASI} = \max_{k_{\min}\le k\le k_{\max}} |R(k)|, \tag{28}$$

where $M = 1001$ is the number of parameter samples, $k_{\min} = 5$, and $k_{\max} = \lfloor M/2 \rfloor$. These bounds exclude very short-range correlations between neighboring parameter samples while avoiding large-lag estimates with insufficient overlap. LASI takes values in $[0, 1]$, with larger values indicating stronger in-phase or antiphase repetition at a nonzero lag. LASI is an empirical index introduced for numerical comparison in this study rather than a rigorous dynamical invariant.

As shown in Fig. 15(a), LASI for the exponentially decaying oscillatory family increases rapidly with α and forms an approximately uniform high-value plateau for relatively large α. The effect of ω is weaker, although periodic band-shaped variations remain clearly visible. In Fig. 15(b), LASI for the algebraically decaying oscillatory family increases more gradually with γ. Its frequency dependence also exhibits alternating bands, but the alternation is comparatively less regular than that of the exponentially decaying family.

This difference originates from competition between the additional oscillatory term and the underlying periodic parameter structure. The basic sine map has an exact period-2 parameter skeleton with respect to μ. As the decay rate increases, the additional oscillatory term weakens, and the underlying repeated structure of the LE spectrum is gradually restored. Because the exponential envelope decays rapidly, a high-value plateau is reached earlier within the scanned parameter range. In contrast, the long tail of the algebraic envelope allows the perturbation-induced nonexact periodic deformation to persist over a broader parameter range. Thus, the

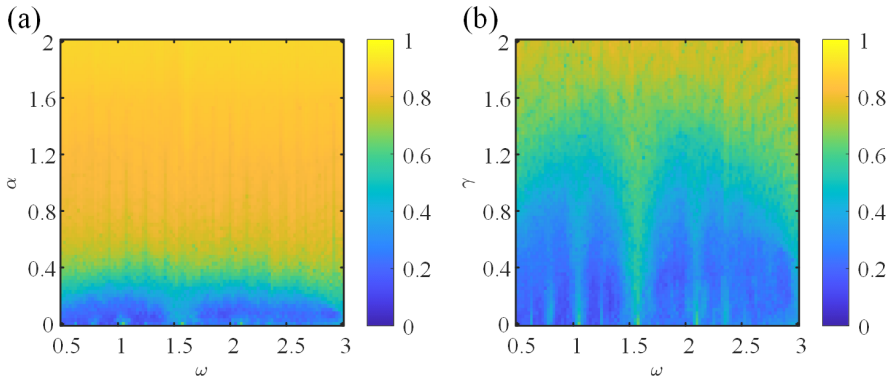


Figure 15: LASI for different oscillatory decay laws. (a) Exponentially decaying oscillatory family, (b) algebraically decaying oscillatory family. L_i is computed with a step size of 0.02, while α, γ, and ω are sampled in steps of 0.025. The LE is evaluated using the last 2×10^4 of 10^5 iterations after discarding transients.

decay law primarily determines the persistence range of perturbation-induced structural deformation along the parameter axis and the rate at which the underlying periodic skeleton is recovered. The oscillation frequency further determines the form of local bands and alternating peaks and valleys.

5. PRNG design

PRNGs play an indispensable role in secure communication, data encryption, and numerical simulation. To convert the chaotic sequence into a uniformly distributed byte stream for cryptographic applications, this paper adopts a quantization strategy based on multiscale quantization and spatial diffusion. The chaotic state is magnified at different decimal depths to extract sensitive low-order information, while differential features are used to reduce phase-space correlations.

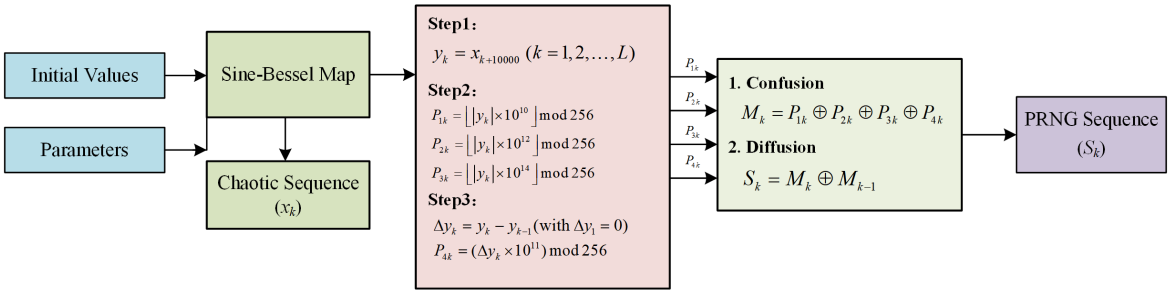


Figure 16: Flowchart of the proposed PRNG system.

The construction of the PRNG based on the Sine-Bessel map is shown in Fig. 16. First, with the parameters $A = 5$, $B = 1$, $a = 0$, $b = 1$ and the initial value $x_0 = 0.1$, the proposed map is iterated, and the initial transient samples are discarded to obtain an effective chaotic sequence. Then, multiscale quantization is performed on the chaotic sequence to extract multiple byte-level feature streams. Meanwhile, a differential sequence is introduced and quantized to reduce the correlation between adjacent phase-space states. Subsequently, the extracted feature streams are combined through bitwise XOR operation to generate a mixed sequence. Finally, cyclic diffusion is applied to further weaken the dependency between neighboring bytes, and the resulting sequence is

Table 3: NIST SP 800-22 test results for the PRNG based on the Sine-Bessel map.

Test	p-value	Pass rate	Result
Frequency	0.9463	98%	Pass
Block frequency	0.6163	99%	Pass
Cumulative sums	0.2133	98%	Pass
Runs	0.5141	98%	Pass
Longest run	0.9963	99%	Pass
Rank	0.8165	99%	Pass
FFT	0.5544	99%	Pass
Non-overlapping template	0.9716	100%	Pass
Overlapping template	0.6371	100%	Pass
Universal	0.1373	100%	Pass
Approximate entropy	0.6993	99%	Pass
Random excursions	0.3838	100%	Pass
Random excursions variant	0.5341	100%	Pass
Serial	0.5955	100%	Pass
Linear complexity	0.2896	99%	Pass

Table 4: Key-sensitivity results of the proposed PRNG.

Key variable	Perturbation	Hamming distance
a	10^{-13}	0.500160
b	10^{-13}	0.500126
x_0	10^{-13}	0.499987

taken as the final pseudorandom sequence.

To evaluate the randomness of the generated sequence, the internationally recognized NIST SP 800-22 statistical test suite is adopted [40,41]. This test suite covers 15 statistical items, including the frequency test, block frequency test, cumulative sums test, and approximate entropy test. A sequence is considered to have good randomness when the p-value is greater than 0.01 and the passing rate lies within the corresponding confidence interval. As shown in Table 3, all generated sequences satisfy the NIST criteria, indicating the potential of the proposed map for pseudorandom sequence generation.

To further characterize the proposed PRNG beyond statistical randomness, the phase parameters and initial condition are considered as the key variables, denoted by $K = (a, b, x_0)$, while the remaining system parameters are fixed. Considering the exact period-2 parameter symmetry with respect to a, the nonredundant interval $a \in [0, 2)$ is adopted, together with $b \in [0, 5]$ and $x_0 \in (0, 1)$. With an effective numerical resolution of $\delta = 10^{-13}$, the nominal key space is estimated as $N_{\text{key}} = \frac{2}{\delta}\frac{5}{\delta}\frac{1}{\delta} \approx 10^{40} \approx 2^{133}$, corresponding to approximately 133 bits.

Key sensitivity was further evaluated by perturbing each key variable independently by 10^{-13} while keeping the remaining variables unchanged. The normalized bitwise Hamming distances between the original and perturbed output sequences are listed in Table 4. All values are close to 0.5, indicating high sensitivity of the generated sequence to small changes in the tested key variables.

6. Conclusion

This paper proposes a one-dimensional Sine-Bessel chaotic map by coupling a sine function with the zeroth-order Bessel function of the first kind. Theoretical analysis establishes the existence and boundedness of the fixed points and derives a local stability criterion. Furthermore, comprehensive dynamical evaluations confirm that the Sine-Bessel chaotic map features broad chaotic regions, high complexity, reduced periodic windows, and robust randomness. Under synchronous translation of both phase parameters, the Bessel term breaks this exact periodicity, producing recurrent but nonidentical bifurcation and LE structures. More generally, a nontrivial decay term coupled with a periodic base function destroys global exact parameter periodicity, although the map-level deviation between adjacent nominal periods tends to zero on bounded state intervals. Comparisons among different decay functions show that the fixed-translation difference governs the persistence of structural deformation, while oscillatory properties determine its alternating form. A PRNG based on the proposed chaotic map also satisfies the adopted NIST SP 800-22 statistical criteria, demonstrating its potential for pseudorandom sequence generation. It should be noted that the numerical observations are based on the investigated parameter ranges and initial conditions, while the NIST tests evaluate statistical randomness rather than cryptographic security. Future work will investigate the application-level implications of parameter-translation symmetry breaking, together with finite-precision effects, predictability, and cryptographic security.

Acknowledgments

This work was supported by the National Natural Science Foundation of China (Nos. 62471496, 62071496), and the Innovation Project of Graduate of Central South University (Nos. 2026ZZTS0847).

Conflict of Interest

The authors declare that they have no conflict of interest.

Data Availability

The data that support the findings of this study are available from the corresponding author upon reasonable request.

References

[1] May R M 1976 *Nature* **261** 459

[2] Rajpathak B, Pillai H K and Bandyopadhyay S 2012 *Chaos* **22** 033126

[3] Du R H, Wang S J, Jin T and Qu S X 2018 *Chin. Phys. B* **27** 100502

[4] Lawnik M, Moysis L, Baptista M S and Volos C 2024 *Nonlinear Dyn.* **112** 6679

[5] Tang Z Q, He S B, Wang H H, Sun K H, Yao Z and Wu X M 2024 *Chin. Phys. B* **33** 030503

[6] Wang H H, Zhu H H, Li B L, Sun K H and Liu W H 2024 *Eur. Phys. J. Plus* **139** 826

[7] Liu S C, Li Y X, Ge X Z, Li C B and Zhao Y B 2022 *Phys. Scr.* **97** 085210

[8] Yu F, Xu S, Lin Y, Gracia Y M, Yao W and Cai S 2024 *Int. J. Bifurcation Chaos* **34** 2450068

[9] Bao H, Su Y H, Hua Z Y, Chen M, Xu Q and Bao B C 2024 *IEEE Trans. Circuits Syst. I-Regul. Pap.* **71** 4145
[10] Inam S, Kanwal S, Rashid S, Hajjej F and Hamdi M 2025 *Eur. Phys. J. Plus* **140** 387
[11] Yu F, Wang X Q, Guo R Y, Ying Z J, He Y and Zou Q 2025 *Chin. Phys. B* **34** 120501
[12] Yu F, Guo R Y, Zheng M F, Yao W, Zhang D D and Cai S 2026 *Chaos Solitons Fractals* **210** 118626
[13] Liu W H, Sun K H, Wang H H and Li B L 2024 *IEEE Trans. Ind. Electron.* **71** 13002
[14] Zhu W T, Sun K H, Li B L and Wang H H 2024 *Phys. Scr.* **99** 065205
[15] Lawnik M and Moysis L 2026 *Nonlinear Dyn.* **114** 203
[16] Qian Y N, Zheng J and Hu H P 2025 *Nonlinear Dyn.* **113** 4815
[17] Zhou M J, Li G D, Pan H P and Song X M 2025 *Chaos Solitons Fractals* **194** 116227
[18] Gao S, Iu H H-C, Wang M J, Jiang D H, Abd El-Latif A A, Wu R and Tang X L 2024 *IEEE Internet Things J.* **11** 21807
[19] Liang Z W, Sun K H and He S B 2021 *Eur. Phys. J. Plus* **137** 51
[20] Liu W H, Sun K H, Wang H H and Liu J 2025 *Nonlinear Dyn.* **113** 33953
[21] Bao H, Li H Z, Hua Z Y, Xu Q and Bao B C 2022 *IEEE Trans. Ind. Inform.* **19** 2792
[22] Hua Z Y, Jin F, Xu B X and Huang H J 2018 *Signal Process.* **149** 148
[23] Zhang S H, Wang C and Zhang H L 2024 *Int. J. Bifurcation Chaos* **34** 2430001
[24] Long G Q, Chai X L, Gan Z H, Jiang D H, He X and Sun M G 2023 *Chaos Solitons Fractals* **176** 114111
[25] Li B L, Sun K H, Wang H H and Liu W H 2024 *Phys. Scr.* **99** 075274
[26] Ibrahim F, Jamil M K, Alali A S and Javed A 2026 *Eur. Phys. J. Plus* **141** 335
[27] Moysis L, Lawnik M, Baptista M S, Volos C and Fragulis G F 2025 *Nonlinear Dyn.* **113** 14103
[28] Hua Z Y, Zhou B H and Zhou Y C 2018 *IEEE Trans. Ind. Electron.* **66** 1273
[29] Natiq H, Banerjee S and Said M R M 2019 *Eur. Phys. J. Spec. Top.* **228** 185
[30] Sun Q K, He S B, Sun K H and Wang H H 2022 *Chin. Phys. B* **31** 120501
[31] Li X F, Chu Y D and Zhang H 2012 *Chin. Phys. B* **21** 030203
[32] Liu W H, Sun K H, Wang H H, Li B L and Chen Y J 2024 *IEEE Trans. Circuits Syst. I-Regul. Pap.* **72** 254
[33] Zhang Z Q, Zhu H, Ban P X, Wang Y and Zhang L Y 2022 *IEEE Trans. Ind. Electron.* **70** 2916
[34] Toktas A, Erkan U, Gao S and Pak C 2024 *Appl. Math. Comput.* **462** 128340
[35] Cho Y-K and Chung S-Y 2021 *J. Math. Anal. Appl.* **500** 125166
[36] Luo A C J 2021 *Int. J. Dyn. Control* **9** 1
[37] Mao X G, Shang P J, Wang J and Ma Y 2018 *Chaos* **28** 113106
[38] Demir K and Ergün S 2022 *Eur. Phys. J. Plus* **137** 591
[39] Mateos D M, Riveaud L E and Lamberti P W 2017 *Chaos* **27** 083118
[40] Pareschi F, Rovatti R and Setti G 2012 *IEEE Trans. Inf. Forensics Secur.* **7** 491
[41] Ding P, Sun K H and Wang H H 2026 *Mod. Phys. Lett. B* **40** 2650040